Received: 23 May 2024 | Revised: 31 October 2024 | Accepted: 4 November 2024

DOI: 10.1002/pamm.202400135

RESEARCH ARTICLE

Hydrothermal behavior of pure PA 6 and homogenization of discontinuous long carbon fiber-reinforced PA 6

Loredana Kehrer[1] | **Benedikt Scheuring**[2] | **Juliane Blarr**[2] | **Thomas Böhlke**[1]

[1]Karlsruhe Institute of Technology (KIT), Institute of Engineering Mechanics—Continuum Mechanics, Karlsruhe, Germany

[2]Karlsruhe Institute of Technology (KIT), Institute for Applied Materials—Materials Science and Engineering, Karlsruhe, Germany

Correspondence
Loredana Kehrer, Karlsruhe Institute of Technology (KIT), Institute of Engineering Mechanics—Continuum Mechanics, Karlsruhe, Germany.
Email: loredana.kehrer@kit.edu

Funding information
Deutsche Forschungsgemeinschaft, Grant/Award Number: 255730231

Abstract

Polymer-based composites play a crucial role in lightweighting applications by providing resource-efficient semi-structural materials. Among these, polyamides, in particular polyamide 6 (PA 6), serve as widely used matrix materials in various technical applications, especially in fiber-reinforced composites. The mechanical properties and performance of PA 6 are significantly affected by environmental factors such as temperature and humidity. Previous research has investigated the influence of hydrothermal conditions on the mechanical properties of pure PA 6. This study aims to extend the preceding investigations with additional experimental tests. As a preliminary work to later investigate the influence of the fibers on the hydrothermal behavior, discontinuous long carbon fiber-reinforced PA 6 is considered for micromechanical modeling of the effective behavior. In this context, a mean-field homogenization approach based on the Hashin–Shtrikman principle is used. By means of a variable reference stiffness, an approach specifically tailored to the material system under consideration can be applied. The simulation data are compared with data from experiments under tension load indicating good agreements for a specific choice of the reference material.

1 | INTRODUCTION

In recent years, the automotive and aircraft industries have experienced a significant increase in the application of polymer-based material systems, driven by their potential as lightweight solutions providing high specific stiffness and strength. These materials, characterized by their processability and cost-effectiveness, enable the construction of tailored structural parts for specific industrial applications, using both discontinuous (DiCo) and continuous fiber-reinforced composites [1]. Thermosets and thermoplastics serve as common polymer matrices in such composites, with thermoplastic polymers exhibiting pronounced thermoviscoelastic properties [2, 3]. Extensive studies have focused on characterizing pure and reinforced polymers in terms of strength [4], damage [5], and cracking behavior [6], as well as on investigating factors such as temperature [7], crystallization [8], and aging [9] effects on material properties. Various approaches have been applied to describe the thermomechanical behavior of thermoplastic-based composites, including the prediction of effective viscoelastic [10], thermoelastic [11], and nonlinear viscoelastic properties [12, 13].

1.1 | Environmental influences on polyamides

Especially in the context of polyamides, the hydrophilic nature, due to the amide functional group in its monomers, results in water absorption when exposed to humid environments, reaching up to 9% of its dry weight [14]. This moisture absorption does not only increase the chain mobility, which affects the glass transition temperature of the material, but also causes significant changes in mechanical properties during sorption [15]. In addition, the polymer swells as water molecules diffuse, pushing chain molecules apart [16]. Depending on the operating conditions, polyamide can absorb or release moisture, affecting its performance. Recent experimental results have shown drying of injection molded polyamide 6 (PA 6) samples during relaxation tests, highlighting the moisture behavior of the material [17, 18]. Ishisaka and Kawagoe [19] examined the time-water superposition of PA 6 at various relative humidity (RH) levels. They discovered that the shift factor follows the Williams-Landel-Ferry (WLF) equation. At temperatures below 0°C, an increase in moisture leads to an increase in the elastic modulus, exhibiting anti-plasticization behavior. In contrast, at temperatures above 0°C, higher moisture levels result in a decrease in the elastic modulus, indicating plasticization behavior. Engelhard and Lion developed an approach to model the humidity-dependent viscoelastic behavior in ref. [20]. Lion and Johlitz present a general approach to thermodynamically consistent modeling of the diffusion processes in ref. [21].

In real-world applications, polymer materials are exposed to harsh environmental conditions that can cause damage. Among these damage mechanisms, photodegradation caused by ultraviolet (UV) radiation leads to photo-oxidative aging of the polymer. During this photo-induced process, the polymer chains break and produce free radicals which ultimately leads to a reduction in molecular mass [22]. Since polymer aging results in irreversible changes in polymer properties such as loss of ductility or reduction in strength, the study of environmental effects on the polymer is critical to assessing long-term performance [23]. However, polymer aging is the cumulative effect of irreversible changes in polymer properties due to exposure to temperature, radiation, moisture, and oxygen [24]. Thus, the combined effect of multiple aging conditions, especially UV exposure, can lead to severe and accelerated degradation and damage. Such a combination is given by UV and water: Water alone typically does not cause significant degradation compared to UV exposure, while UV exposure alone has a pronounced effect on the surface. The combined exposure, though, results in synergistic aging [25]. In this work, however, UV exposure is not yet considered, but is the subject of future research and, thus, briefly addressed here.

1.2 | Fiber-reinforced composites

Predicting macroscopic properties while accounting for microscopic heterogeneities is a prevailing research focus. Modern characterization techniques provide detailed microstructural information that is used in homogenization methods to describe the material behavior. Mean-field methods can be categorized into bounds and estimates for macroscopic behavior prediction. Voigt and Reuss [26, 27] formulated upper and lower bounds in the context of linear elastic material behavior for polycrystals based on the minimum potential and complementary energy principle [28]. First-order bounds, considering only the volume fraction, were introduced by Hashin and Shtrikman [29] to include average geometrical properties of inclusions, with Willis [30, 31] proposing a generalized formulation. Kröner [32] derived higher-order bounds, which were applied to particulate and fibrous composites by Milton [33] and Torquato [34]. Castañeda [35] extended the Hashin–Shtrikman principle to nonlinear behavior, with applications to anisotropic polycrystalline materials by Böhlke and Lobos [36]. Approximation methods based on Eshelby's solution [37], such as the Mori and Tanaka method [38], have found wide application, although limited in certain cases [39]. Recent studies employ a two-step homogenization technique that divides a domain into subdomains with two phases [40, 41]: the matrix and the inclusion medium. First, each subdomain undergoes individual homogenization, often using the Mori-Tanaka scheme [42]. Subsequently, the overall properties are computed by averaging over all domains, often using the Voigt and Reuss methods for their simplicity [43]. Given the general limitations of the Mori–Tanaka scheme in its application, this work uses a Hashin–Shtrikman based method as two-step homogenization instead.

1.3 | Contents and originality

In general, the present work is structured as follows: First, the environmental influence of humidity on the thermoviscoelastic material properties of pure PA 6 is studied by dynamic mechanical analysis (DMA). Then, a

carbon fiber-reinforced composite with PA 6 as matrix material is considered in a micromechanical approach. A Hashin–Shtrikman based mean-field model is used to calculate the effective elastic properties.

In addition to previous investigations such as the analysis of the mechanical behavior through static tests as in ref. [18], special emphasis is placed here on temperature-frequency tests, which reveal shifts in characteristic properties such as the glass transition temperature, as well as plasticization and anti-plasticization effects at temperatures above and below 0°C. With respect to the micromechanical modeling, the Hashin–Shtrikman based two-step approach provides a tailored method that is particularly suitable when the phase contrast is high. The orientation dependence is addressed by orientation tensors applied to carbon-reinforced PA 6. The fibers are considered to exhibit isotropic (ISO) material symmetry as a first approximation of the material properties due to the lack of transversely ISO material properties.

1.4 | Notation

The current paper employs a direct tensor notation following Truesdell and Toupin [44]. Scalar quantities are indicated by lowercase letters (e.g., a), while vectors are denoted by lowercase bold letters (e.g., $\boldsymbol{a}$). A second-order tensor is represented by $\boldsymbol{A}$, and a fourth-order tensor by $\mathbb{A}$. Scalar and dyadic products are denoted by $\boldsymbol{A} \cdot \boldsymbol{B}$ and $\boldsymbol{A} \otimes \boldsymbol{B}$, respectively. The composition of two tensors of the same order is indicated by $\boldsymbol{AB}$ and $\mathbb{AB}$, while a linear mapping is represented as $\boldsymbol{A} = \mathbb{C}[\boldsymbol{B}]$. Additionally, the box product is defined as $(\boldsymbol{A}\square\boldsymbol{B})[\boldsymbol{C}] = \boldsymbol{ACB}$. The major transposition of a fourth-order tensor $\mathbb{A}^{\mathsf{T}}$ is expressed as $A^{\mathsf{T}}_{ijkl} = A_{klij}$ in index notation. The symmetric identity tensor of fourth-order is denoted by $\mathbb{I}^{\mathsf{S}}$, and of second order by $\boldsymbol{I}$. The brackets $\langle\cdot\rangle$ denote the ensemble average, corresponding to volume averaging in an infinite volume limit for ergodic media, and are defined for a quantity ψ by $\langle\psi\rangle = \sum_{\gamma=1}^{N} c_\gamma \psi_\gamma$, with c_γ denoting the volume fraction of phase γ. Macroscale quantities are indicated by a superimposed bar, for example, $\bar{\boldsymbol{\sigma}}$.

2 | DMA

2.1 | Experimental setup

The thermoviscoelastic properties of materials can be assessed using DMA. The experiments conducted in this study utilize the GABO Eplexor500N. The basic principles and equations are briefly outlined below, with a comprehensive overview provided by ref. [45]. In DMA, a sample undergoes a cyclic loading of either strain or stress. In terms of an axial strain load $\varepsilon(t)$, it consists of a static preload $\varepsilon_{\text{stat}} = \varepsilon_0$ superimposed by a sinusoidal oscillation $\varepsilon_{\text{dyn}} = \Delta\varepsilon \sin(\omega t)$, where $\Delta\varepsilon$ represents the amplitude and ω the frequency of the cyclic load, reading

$$\varepsilon(t) = \varepsilon_{\text{stat}} + \varepsilon_{\text{dyn}} = \varepsilon_0 + \Delta\varepsilon \sin(\omega t). \tag{1}$$

During the test, both the sample's deformation amplitude and the phase shift δ between the cyclic load and the material's response are measured and given by

$$\sigma(t) = \sigma_0 + \Delta\sigma \sin(\omega t + \delta). \tag{2}$$

The storage modulus E', reflecting the instantaneous elastic response of the material to the oscillation, and the loss modulus E'', indicating the viscous behavior due to internal friction, can be determined by

$$E' = \frac{\Delta\sigma}{\Delta\varepsilon}\cos(\delta), \quad E'' = \frac{\Delta\sigma}{\Delta\varepsilon}\sin(\delta), \quad \tan\delta = \frac{E''}{E'}, \tag{3}$$

with $\tan\delta$ indicating the loss factor. By subjecting the sample to varying temperature and frequency loads, the thermoviscoelastic properties of the material can be determined.

2.2 | Sample preparation

This study focuses on two sample states: dry-as-molded (DAM) and standard atmosphere (ATM-23/50) conditioned samples. DAM samples exhibit a nominal equilibrium moisture content below 0.3 wt.% and are typically observed directly after

TABLE 1 Test parameters for temperature-frequency tests by DMA.

Test parameter	Value
Static load	$\varepsilon_0 = 0.1\%$
Dynamic load	$\Delta\varepsilon = 0.05\%$
Frequency	$f \in [0.5, 50]$ Hz
Temperature	$\vartheta \in [-100, 150]°C$

Abbreviation: DMA, dynamic mechanical analysis.

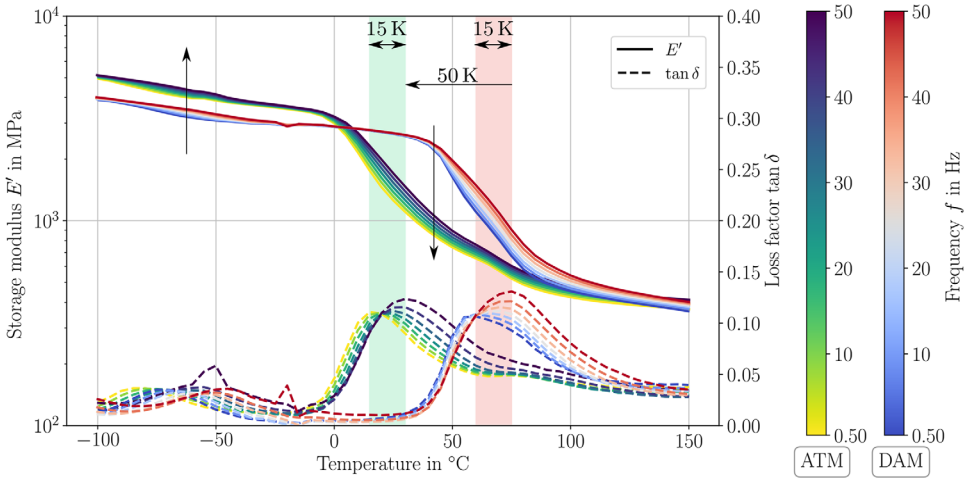

FIGURE 1 Temperature-frequency tests for DAM and ATM-23/50 samples indicate not only a thermoviscoelastic material behavior for both conditioning states of the samples but also a plasticization effect for moister samples and higher temperatures and an anti-plasticization effect for temperatures below 0°C (visualized by the vertical arrows). Furthermore, the glass transition is shifted by 50 K from higher temperatures to lower temperatures for the ATM-23/50 sample. DAM, dry- as- molded..

manufacturing. To maintain this condition, the samples can either be stored in desiccators or vacuum bags. In our study, samples are vacuum oven-dried and then stored in a desiccator. Additionally, conditioned samples are relevant for certain industrial applications, aiming for specific water absorption levels. Standard atmospheres vary based on application and polymer, representing average lab conditions with an equilibrium moisture content between 2.5 wt.% and 3.0 wt.%. The ISO 291 standard [46] defines the ATM-23/50 conditions for 23°C and 50% RH. Given that the moisture equilibrium state for PA 6 may only be reached after an extended period of time, up to one year for a sample thickness of 2 mm, an accelerated conditioning program, such as that proposed by ref. [47] is employed. Conditioning of samples is conducted at 55°C and 50%RH (ATM-55/50) for a minimum of 7 days. Equilibrium is confirmed if weight measurements exhibit a variation of less than 0.1% between three consecutive measurements. Once equilibrium has been reached, samples are stored at ATM-23/50 conditions for future use. In this work, the ATM-23/50 and ATM-55/50 conditions are achieved in the samples using a climatic chamber (Memmert ICH110 L). Further details are given in ref. [17].

2.3 | Temperature-frequency tests

The geometry of the samples for DMA testing are given by 83 mm × 10 mm × 2 mm with respect to length, width, and thickness. To investigate the thermoviscoelastic material behavior, frequency load and temperature are varied as listed in Table 1 for DAM and ATM-23/50 samples. Here, neat PA 6 is considered.

The results of the temperature-frequency tests are depicted in Figure 1. The solid lines show the data for the storage modulus E' and the dashed lines for the loss factor $\tan\delta$ both for DAM and ATM-23/50 conditioned PA 6. In general, a temperature- and frequency-dependent behavior for E' and $\tan\delta$ is detected as is typically observed for polymers. Comparing the DAM and ATM-23/50 conditioned samples, E' of the ATM-23/50 sample is horizontally shifted towards lower temperatures. Moreover, temperatures above 0°C indicate a so-called plasticization effect, while below 0°C, the moister

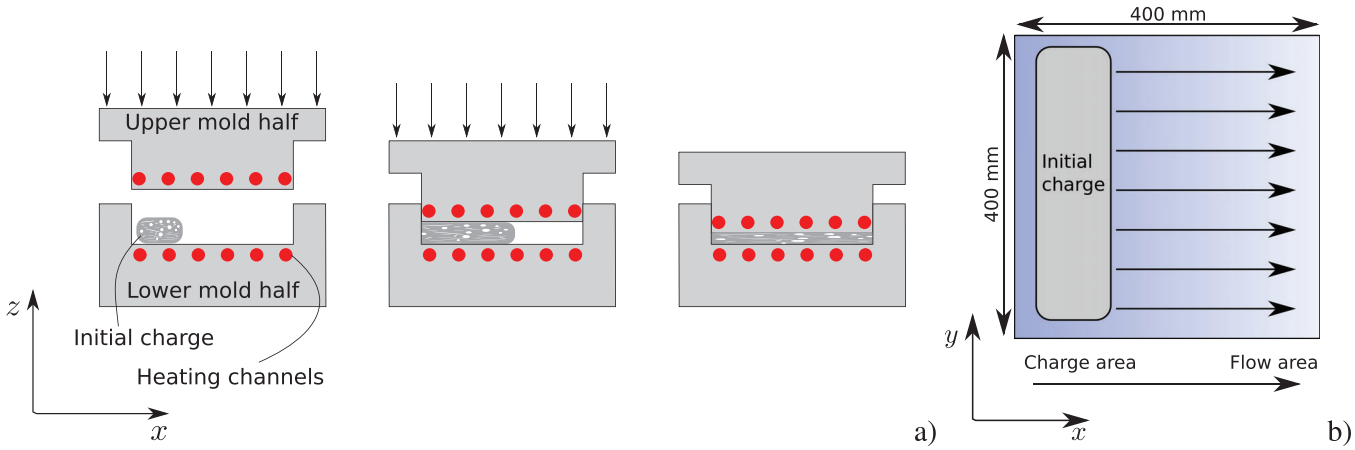

FIGURE 2 Manufacturing of long fiber-reinforced thermoplastics by LFT-D process. (A) LFT plastificate position within the press and (B) resulting plaque after solidification. Pictures adapted from ref. [50].

sample is stiffer compared to the drier sample, indicating an anti-plasticization effect. Similar observations are made in refs. [47, 48]. Depending on the frequency load, the peak value of $\tan\delta$ is shifted by about 15 K, from 75°C to 60°C for the DAM sample, and from 30°C to 15°C for the ATM-23/50 sample. Considering the peak in the $\tan\delta$ distribution as a characteristic for the glass transition temperature θ_g, it is noted that θ_g is shifted by about 50 K from higher to lower temperatures when the moisture level is increased.

3 | DiCo CARBON FIBER-REINFORCED PA 6

3.1 | LFT-D process

Plaques are manufactured from long fiber-reinforced thermoplastics in the direct process (LFT-D)s at the Fraunhofer ICT (Pfinztal, Germany) on a LFT-D machine by Dieffenbacher (Dieffenbacher GmbH, Germany). The LFT-D process starts with the production of an LFT plastificate, whereby polymer pellets are introduced into a screw extruder, facilitating the melting of the polymer, compare ref. [49]. Subsequently, within a second screw extruder, the molten polymer undergoes mixing with continuous fiber rovings, while the extruder consistently pulls the fiber through rotational movement. During this process, the fiber rovings undergo shearing, impregnation, and distribution. The thoroughly mixed composite strand is then discharged onto a heated conveyer belt, where it is cut into long plastificates. Following this, the plastificate is transferred to a hydraulic press, positioned at one end, and pressed into plaques, from which samples can be extracted after the solidification, compare ref. Figure 2. Samples are extracted from the plaques in different directions relative to the flow direction by water jet cutting and re-dried in a vacuum oven. Details are given in ref. [50].

3.2 | CT analysis

Samples at different positions on a plaque, as shown in Figure 2B, are examined by CT analysis. A slice of a reconstructed volumetric CT image is shown as an example in Figure 3. For further analysis, the CT images are subjected to a 3D orientation analysis based on the structure tensor, compare refs. [51, 52]. Fibers with different orientations are highlighted with different colors within the HSV color spectrum. Here, the orientation analysis is performed for different positions on the plaque and an overall value as the average fiber orientation is considered for later simulations. Details on CT and microstructure analysis are given in ref. [50]. The orientation analysis reveals a predominantly planarisotropic (PI) distribution, as indicated by the relatively small magnitude of the third eigenvalue of the orientation tensor compared to the other two eigenvalues. In Figure 3B, the largest eigenvalue is plotted against the second largest eigenvalue. This gives a rough indication of the average orientation of the fibers in the material.

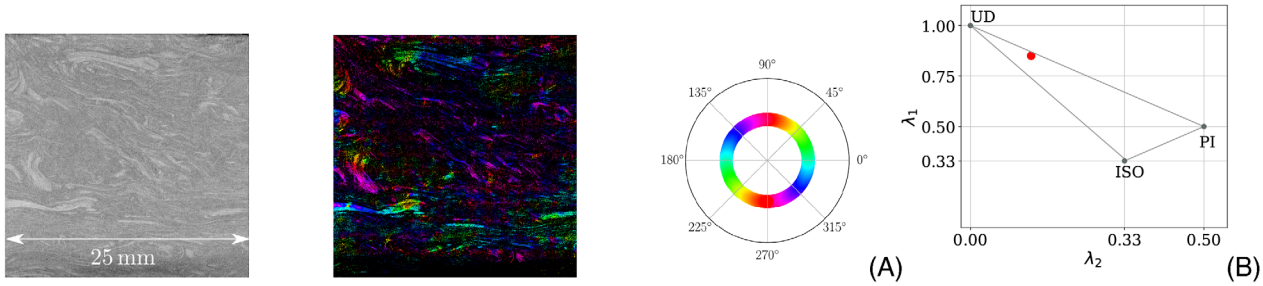

FIGURE 3 (A) Reconstructed CT scan of a carbon fiber-reinforced PA 6 sample with orientation analysis. Differently oriented fiber are indicated by different colors within the HSV (hue, saturation and value) color spectrum. Pictures adapted from ref. [50]. (B) First and second eigenvalue of the orientation tensor of second order are depicted for a mean orientation representation of the sample within the cured plaque, compare ref. [50]. The red dot represents the given mean orientation of the data compared to the special cases of UD, PI, and ISO orientation. CT, computed tomography; ISO, isotropic; PA 6, polyamide 6; PI, planar isotropic; UD, unidirectional.

4 | EFFECTIVE ELASTIC MATERIAL PROPERTIES OF CARBON FIBER-REINFORCED PA 6

4.1 | Mean-field homogenization by Hashin–Shtrikman two-step method

The equations for the mean-field homogenization of the fiber-reinforced composite are presented in the following. On the microscopic level, the composite is assumed to consist of matrix and fiber material with phasewise constant material properties. Additionally, it is assumed that both the fiber and matrix material exhibit ISO material symmetry. Thus, the stiffness tensor of fourth order $\mathbb{C}$ is given for each phase α by $\mathbb{C}_\alpha = 3K_\alpha \mathbb{P}_1 + 2G_\alpha \mathbb{P}_2$ in terms of the compression modulus K, the shear modulus G, and the first and second fourth-order projector $\mathbb{P}_1 = \boldsymbol{I} \otimes \boldsymbol{I}/3$ and $\mathbb{P}_2 = \mathbb{I}^{\mathrm{S}} - \mathbb{P}_1$. The microstructure is characterized by geometric characteristics such as the fiber volume content c_{F}, the fiber length l_{F}, and the mean fiber orientation in terms of fiber orientation tensors of second and fourth order, $\boldsymbol{N}$ and $\mathbb{N}$, respectively. By means of Hooke's law, the effective elastic behavior on macroscopic scale is determined by $\bar{\boldsymbol{\sigma}} = \langle \boldsymbol{\sigma} \rangle = \langle \mathbb{C}[\boldsymbol{\varepsilon}] \rangle$, with $\boldsymbol{\sigma}$ denoting the Cauchy stress tensor and $\boldsymbol{\varepsilon}$ the infinitesimal strain tensor. The local strains on microscopic level are generally related to the applied external strains on macroscopic level by means of the mechanical strain localization tensor $\mathbb{A}$, reading $\boldsymbol{\varepsilon} = \mathbb{A}[\bar{\boldsymbol{\varepsilon}}]$. The effective stiffness can then be determined by $\bar{\mathbb{C}} = \langle \mathbb{C}\mathbb{A} \rangle$.

Various homogenization methods are derived based on assumptions for the choice of $\mathbb{A}$. Considering fiber-reinforced composites, the fibers are often modeled as ellipsoidal-shaped inclusions and are micromechanically accounted for by means of Hill's polarization tensor $\mathbb{P}_0$, for example, compare ref. [53].

In the previous work [11], a two-step homogenization method, based on the Hashin–Shtrikman approach, is introduced for analyzing two-phase composite materials. The method incorporates formulations by Walpole [53] and Willis [31] to account for eigenstrains.

In this approach, the entire volume is divided into distinct regions, each containing one or more fibers with a specific orientation, embedded within the matrix material. The number of regions is equal to the number of distinct fiber orientations. For each region with a unidirectional (UD) structure, Hill's polarization tensor $\mathbb{P}^{\mathrm{UD}}$ is explicitly defined, compare refs. [53, 54]. Effective elastic properties are then determined of each domain γ using the Hashin–Shtrikman principle, yielding upper and lower bounds, reading

$$\bar{\mathbb{C}}_\gamma^{\mathrm{UD}+} = \mathbb{C}_\gamma + c_{\mathrm{M}}(\mathbb{C}_{\mathrm{M}} - \mathbb{C}_\gamma)\left(\mathbb{I}^{\mathrm{S}} + c_\gamma \mathbb{P}_\gamma^{\mathrm{UD}}(\mathbb{C}_{\mathrm{M}} - \mathbb{C}_\gamma)\right)^{-1}, \tag{4}$$

$$\bar{\mathbb{C}}_\gamma^{\mathrm{UD}-} = \mathbb{C}_{\mathrm{M}} - c_\gamma(\mathbb{C}_{\mathrm{M}} - \mathbb{C}_\gamma)\left(\mathbb{I}^{\mathrm{S}} - c_{\mathrm{M}} \mathbb{P}_\gamma^{\mathrm{UD}}(\mathbb{C}_{\mathrm{M}} - \mathbb{C}_\gamma)\right)^{-1}, \tag{5}$$

with c_γ and c_{M} denoting the volume fraction of domain γ and the matrix material, respectively. In the second step, the total effective stiffness is computed by averaging over all domains

$$\bar{\mathbb{C}}^{\mathrm{HS}\pm} = \mathbb{C}_0 - \mathbb{P}_0^{-1} + \left\langle \frac{1}{c_{\mathrm{F}}} (\mathbb{P}_0^{-1} + \bar{\mathbb{C}}^{\mathrm{UD}\pm} - \mathbb{C}_0)^{-1} \right\rangle^{-1} = \mathbb{C}_0 - \mathbb{P}_0^{-1} + \langle \mathbb{A}^* \rangle_{\mathrm{oa}}^{-1}. \tag{6}$$

TABLE 2 Mechanical and dimension parameters for the fiber and matrix material used for the homogenization scheme, compare ref. [50].

Parameter	Matrix material	Fiber material
Young's modulus	$E_M = 3.1\,\text{GPa}$	$E_F = 202\,\text{GPa}$
Poisson's ratio	$\nu_M = 0.386$	$\nu_F = 0.2$
Volume fraction	$c_M = 0.765$	$c_F = 0.235$
Aspect ratio	—	$a_F = 220$

The subscript oa denotes the orientation averaging as presented in ref. [55], and c_F represents the volume fraction of the fibers within the composite. The material behavior is modeled assuming ISO two-point correlation of the domains, with the reference stiffness formulated as a variable parameter k, ranging from 0 to 1 to encompass the matrix and fiber stiffness

$$\mathbb{C}_0 = (1-k)\mathbb{C}_M + k\,\mathbb{C}_F,\ k \in [0,1]. \tag{7}$$

The resulting expressions feature transversely ISO tensors, allowing to account for the mean orientation of the microstructure by using second- and fourth-order orientation tensors [55], reading

$$\langle \mathbb{A}^* \rangle_{oa} = b_1 \mathbb{N} + b_2(\boldsymbol{N}\otimes\boldsymbol{I} + \boldsymbol{I}\otimes\boldsymbol{N}) + b_3(\boldsymbol{N}\square\boldsymbol{I} + (\boldsymbol{N}\square\boldsymbol{I})^{T_R} + (\boldsymbol{I}\square\boldsymbol{N})^{T_H} + (\boldsymbol{I}\square\boldsymbol{N})^{T_R}) + b_4\boldsymbol{I}\otimes\boldsymbol{I} + b_5\mathbb{I}^S, \tag{8}$$

with $b_1 = A^*_{1111} + A^*_{2222} - 2A^*_{1122} - 4A^*_{1212}$, $b_2 = A^*_{1122} - A^*_{2233}$, $b_3 = A^*_{1212} + (A^*_{2233} - A^*_{2222})/2$, $b_4 = A^*_{2233}$, and $b_5 = A^*_{2222} - A^*_{2233}$.

A detailed derivation of the mean-field model and application to long fiber-reinforced sheet molding compound composites can be found in ref. [11].

4.2 | Comparison of simulation and experimental results

The experimental data presented in this section are documented in ref. [50] and used here for the comparison with the simulation results. In this context, DAM samples are considered. Table 2 lists the parameters used for the mean-field homogenization.

Young's modulus of the fiber material was tested at the FIBRE institute in Bremen for single fibers in longitudinal direction. Since no experimental data are available for the transversely ISO material properties of the carbon fibers, Young's modulus and Poisson's ratio are used as ISO material parameters for the fiber material as rough approximation. In this context, the Hashin–Shtrikman two-step method is used and evaluated for the lower bound in the first step according to Equation (5). Since the upper bound according to Equation (4) yields results that show significant deviations from experimental data, only results for the lower bound in the first step are presented, here. To compare simulation results with experimental data, the orientation-dependent Young's modulus is determined based on the effective stiffness tensor by $\bar{E}(\boldsymbol{d}) = (\boldsymbol{d}\otimes\boldsymbol{d}\cdot\bar{\mathbb{C}}^{-1}[\boldsymbol{d}\otimes\boldsymbol{d}])^{-1}$, compare ref. [56]. In Figure 4, the effective Young's modulus in the $x-y$ plane is depicted, that is, $\bar{E}(\pi/2,\varphi)$. This coincides with the coordinates depicted in Figure 2B: 0° corresponds to the x-direction and 90° to the y-direction, respectively. Moreover, the experimental data from tests under tension load are depicted by red dots for differently oriented samples.

For the simulation results, there is a clear dependency on parameter k which influences the effective stiffness through the reference stiffness. In the present investigations, a good agreement for differently oriented samples and their respective experimental data is given for the choice of $k = 0.1$ which corresponds to a reference stiffness that is near the material properties of the matrix stiffness. This emphasizes the advantage of this approach since a tailoring to the specific material system is possible.

5 | SUMMARY AND CONCLUSION

In the present study, the influence of moisture on characteristic material properties, in particular the glass transition temperature, was investigated using temperature-frequency tests performed via DMA. In addition, a shift in the ther-

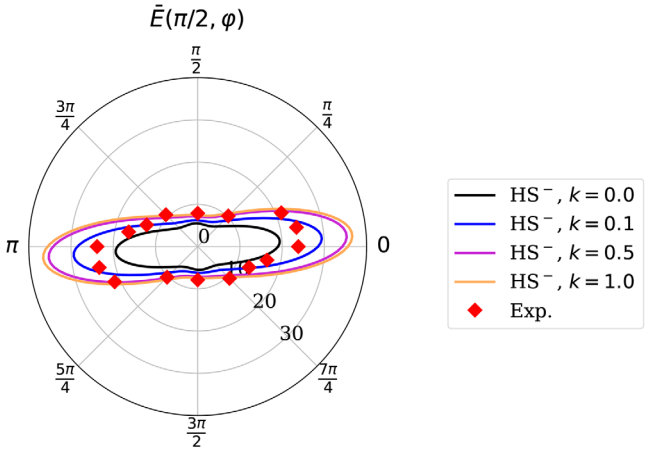

FIGURE 4 Orientation-dependent effective Young's modulus depicted in the contour plot for the $x - y$ plane. The solid lines correspond to the simulation results obtained for different parameters k of the Hashin–Shtrikman two-step method. The red dots represent data obtained from experiments under tension load. For a reference stiffness close to the matrix material properties, a good agreement between simulation results and experimental data for different sample orientations are achieved.

moviscoelastic material behavior induced by varying the equilibrium moisture content within the sample was observed, complementing the drying effects observed in relaxation tests in previous investigations [17, 18]. Furthermore, at temperatures below 0°C, the results showed an anti-plasticizing effect, while temperatures above 0°C led to plasticization, resulting in a softening of the stiffness. Regarding the carbon fiber-reinforced PA 6, homogenization was performed using ISO fiber properties as a first approximation in the absence of transversely ISO material properties. In a previous work [11], the Hashin–Shtrikman based two-step method was developed, formulated with orientation tensors, and applied to sheet molding compound composites, showing not only good agreement with experimental data, but also the advantage of a tailored approach, compare ref. [57]. Here, by selecting a specific parameter for the reference stiffness, results were obtained that were sufficiently close to the experimental data, indicating the suitability of this tailored approach to a different material system. Currently, the simulations are limited to elastic material properties, as the homogenization scheme does not yet include adjustments for environmental factors such as humidity or temperature. As a preliminary measure, the homogenization scheme is being applied to the existing material to enable an initial assessment of the method's suitability. Nevertheless, it is imperative to consider the influence of water and other environmental factors on carbon fiber-reinforced composites in order to gain a comprehensive understanding of their impact on the material behavior. Furthermore, future investigations are needed to include transversely ISO properties for the fiber material to accurately capture the material symmetry properties.

AUTHOR CONTRIBUTIONS

Loredana Kehrer: conceptualization; investigation; experiments; simulation; formal analysis; visualization; writing—original draft. **Benedikt Scheuring**: experiments; visualization; writing—editing and review. **Juliane Blarr**: formal analysis; visualization; writing—editing and review. **Thomas Böhlke**: supervision; funding acquisition; writing—editing and review.

ACKNOWLEDGMENTS

The research documented in this manuscript has been funded by the Deutsche Forschungsgemeinschaft (DFG, German Research Foundation), project number 255730231, within the International Research Training Group "Integrated engineering of continuous-discontinuous long fiber reinforced polymer structures" (GRK 2078/2). The support by the German Research Foundation (DFG) is gratefully acknowledged.

Open access funding enabled and organized by Projekt DEAL.

ORCID

Loredana Kehrer https://orcid.org/0000-0002-5712-6515

REFERENCES

1. Görthofer, J., Meyer, N., Pallicity, T. D., Schöttl, L., Trauth, A., Schemmann, M., Hohberg, M., Pinter, P., Elsner, P., Henning, F., Hrymak, A., Seelig, T., Weidenmann, K., Kärger, L., & Böhlke, T. (2019). Virtual process chain of sheet molding compound: Development, validation and perspectives. *Composites Part B: Engineering*, *169*, 133–147.
2. Tschoegl, N. W. (2012). *The phenomenological theory of linear viscoelastic behavior: An introduction*. Springer Science & Business Media.
3. Shaw, M. T., & MacKnight, W. J. (2018). *Introduction to polymer viscoelasticity*. John Wiley & Sons.
4. Bondy, M., Pinter, P., & Altenhof, W. (2017). Experimental characterization and modelling of the elastic properties of direct compounded compression molded carbon fibre/polyamide 6 long fibre thermoplastic. *Materials and Design*, *122*, 184–196.
5. Trauth, A., & Weidenmann, K. A. (2018). Continuous-discontinuous sheet moulding compounds–Effect of hybridisation on mechanical material properties. *Composite Structures*, *202*, 1087–1098.
6. Schöttl, L., Kolb, P., Liebig, W. V., Weidenmann, K. A., Inal, K., & Elsner, P. (2020). Crack characterization of discontinuous fiber-reinforced composites by using micro-computed tomography: Cyclic in-situ testing, crack segmentation and crack volume fraction. *Computer Communications*, *21*, 100384.
7. Eftekhari, M., & Fatemi, A. (2016). Tensile behavior of thermoplastic composites including temperature, moisture, and hygrothermal effects. *Polymer Testing*, *51*, 151–164.
8. Kállay-Menyhárd, A., Suba, P., László, Z., Fekete, H., Mester, A., Horváth, Z., Varga, J., & Móczó, J. (2015). Direct correlation between modulus and the crystalline structure in isotactic polypropylene. *EXPRESS Polymer Letters*, *9*(3), 308–320.
9. Wudy, K., & Drummer, D. (2016). Aging behavior of polyamide 12: Interrelation between bulk characteristics and part properties. In: *Solid Freeform Fabrication Symposium on Additive Manufacturing*, USA, (pp. 7–10). University of Texas.
10. Pallicity, T. D., & Böhlke, T. (2021). Effective viscoelastic behavior of polymer composites with regular periodic microstructures. *International Journal of Solids and Structures*, *216*, 167–181.
11. Kehrer, L., Wood, J. T., & Böhlke, T. (2020). Mean-field homogenization of thermoelastic material properties of a long fiber-reinforced thermoset and experimental investigation. *Journal of Composite Materials*, *54*(25), 3777–3799.
12. Zink, T., Kehrer, L., Hirschberg, V., Wilhelm, M., & Böhlke, T. (2022). Nonlinear Schapery viscoelastic material model for thermoplastic polymers. *Journal of Applied Polymer Science*, *139*(17), 52028.
13. Keursten, J., Kehrer, L., & Böhlke, T. (2023). Linear and nonlinear thermoviscoelastic behavior of polyamide 6. *Proceedings of Applied Mathematics and Mechanics*, *22*(1), e202200145.
14. Vlasveld, D., Groenewold, J., Bersee, H., & Picken, S. (2005). Moisture absorption in polyamide-6 silicate nanocomposites and its influence on the mechanical properties. *Polymer*, *46*(26), 12567–12576.
15. Sambale, A. K., Maisl, M., Herrmann, H.-G., & Stommel, M. (2021). Characterisation and modelling of moisture gradients in polyamide 6. *Polymers*, *13*(18), 3141.
16. Sharma, P., Sambale, A., Stommel, M., Maisl, M., Herrmann, H.-G., & Diebels, S. (2020). Moisture transport in PA6 and its influence on the mechanical properties. *Continuum Mechanics and Thermodynamics*, *32*(2), 307–325.
17. Kehrer, L., Keursten, J., Hirschberg, V., & Böhlke, T. (2023). Dynamic mechanical analysis of PA 6 under hydrothermal influences and viscoelastic material modeling. *Journal of Thermoplastic Composite Materials*, *36*(11), 4630–4664.
18. Dyck, A., Groß, L., Kehrer, K. J. L., & Böhlke, T. (2024). Modeling and fe simulation of coupled water diffusion and viscoelasticity in relaxation tests of polyamide 6. *Continuum Mechanics and Thermodynamics*, *36*, 935–953.
19. Ishisaka, A., & Kawagoe, M. (2004). Examination of the time–water content superposition on the dynamic viscoelasticity of moistened polyamide 6 and epoxy. *Journal of Applied Polymer Science*, *93*(2), 560–567.
20. Engelhard, M., & Lion, A. (2013). Modelling the hydrothermomechanical properties of polymers close to glass transition. *ZAMM-Journal of Applied Mathematics and Mechanics*, *93*(2–3), 102–112.
21. Lion, A., & Johlitz, M. (2020). On the thermomechanics of solids surrounded by liquid media: Balance equations, free energy and nonlinear diffusion. *Continuum Mechanics and Thermodynamics*, *32*(2), 281–305.
22. Lu, T., Solis-Ramos, E., Yi, Y., & Kumosa, M. (2018). UV degradation model for polymers and polymer matrix composites. *Polymer Degradation and Stability*, *154*, 203–210.
23. Tocháček, J., & Vrátníčková, Z. (2014). Polymer life-time prediction: The role of temperature in UV accelerated ageing of polypropylene and its copolymers. *Polymer Testing*, *36*, 82–87.
24. Markovičová, L., & Zatkalíková, V. (2019). The effect of UV aging on structural polymers, In: IOP Conference Series: Materials Science and Engineering, 012004.
25. de Souza Rios, A., de Amorim Júnior, W. F., de Moura, E. P., de Deus, E. P., & de Andrade Feitosa, J. P. (2016). Effects of accelerated aging on mechanical, thermal and morphological behavior of polyurethane/epoxy/fiberglass composites. *Polymer Testing*, *50*, 152–163.
26. Voigt, W. (1889). Ueber die Beziehung zwischen den beiden Elasticitätsconstanten isotroper Körper. *Annalen der Physik*, *274*(12), 573–587.
27. Reuss, A. (1929). Berechnung der Fließgrenze von Mischkristallen auf grund der Plastizitätsbedingung für Einkristalle. *Journal of Applied Mathematics and Mechanics*, *9*(1), 49–58.
28. Hill, R. (1952). The elastic behaviour of a crystalline aggregate. *Proceedings of the Physical Society of London, Section A*, *65*(5), 349–354.
29. Hashin, Z., & Shtrikman, S. (1962). A variational approach to the theory of the elastic behaviour of polycrystals. *Journal of the Mechanics and Physics of Solids*, *10*(4), 343–352.
30. Willis, J. R. (1977). Bounds and self-consistent estimates for the overall properties of anisotropic composites. *Journal of the Mechanics and Physics of Solids*, *25*(3), 185–202.

31. Willis, J. R. (1981). Variational and related methods for the overall properties of composites. *Advances in Applied Mechanics*, *21*, 1–78.
32. Kröner, E. (1977). Bounds for effective elastic moduli of disordered materials. *Journal of the Mechanics and Physics of Solids*, *25*(2), 137–155.
33. Milton, G. (2002). *The theory of composites, Cambridge monographs on applied and computational mathematics*. Cambridge University Press.
34. Torquato, S. (2002). *Random heterogeneous materials: Microstructure and macroscopic properties*. Springer.
35. Castañeda, P. P. (1991). The effective mechanical properties of nonlinear isotropic composites. *Journal of the Mechanics and Physics of Solids*, *39*(1), 45–71.
36. Böhlke, T., & Lobos, M. (2014). Representation of Hashin–Shtrikman bounds of cubic crystal aggregates in terms of texture coefficients with application in materials design. *Acta Materials*, *67*, 324–334.
37. Eshelby, J. D. (1957). The determination of the elastic field of an ellipsoidal inclusion, and related problems. *Proceedings of the Royal Society A*, *241*(1226), 376–396.
38. Mori, T., & Tanaka, K. (1973). Average stress in matrix and average elastic energy of materials with misfitting inclusions. *Acta Metallurgica et Materialia*, *21*(5), 571–574.
39. Benveniste, Y., Dvorak, G., & Chen, T. (1989). Stress fields in composites with coated inclusions. *Mechanics of Materials*, *7*(4), 305–317.
40. Lielens, G., Pirotte, P., Couniot, A., Dupret, F., & Keunings, R. (1998). Prediction of thermo-mechanical properties for compression moulded composites. *Composites Part A: Applied Science and Manufacturing*, *29*(1–2), 63–70.
41. Camacho, C. W., Tucker, C. L., Yalvaç, S., & McGee, R. L. (1990). Stiffness and thermal expansion predictions for hybrid short fiber composites. *Polymer Composites*, *11*(4), 229–239.
42. Doghri, I., & Tinel, L. (2005). Micromechanical modeling and computation of elasto-plastic materials reinforced with distributed-orientation fibers. *International Journal of Plasticity*, *21*(10), 1919–1940.
43. Doghri, I., & Friebel, C. (2005). Effective elasto-plastic properties of inclusion-reinforced composites. Study of shape, orientation and cyclic response. *Mechanics of Materials*, *37*(1), 45–68.
44. Truesdell, C., & Toupin, R. (1960). The classical field theories. In: *Principles of classical mechanics and field theory* (pp. 226–793). Springer.
45. Menard, K. P. (2008). *Dynamic mechanical analysis: A practical introduction*. CRC press.
46. ISO 291. (2008). *Plastics—Standard atmospheres for conditioning and testing* (ISO 291:2008(E)).
47. Jia, N., Fraenkel, H. A., & Kagan, V. A. (2004). Effects of moisture conditioning methods on mechanical properties of injection molded nylon 6. *Journal of Reinforced Plastics and Composites*, *23*(7), 729–737.
48. Venoor, V., Park, J. H., Kazmer, D. O., & Sobkowicz, M. J. (2021). Understanding the effect of water in polyamides: A review. *Polymer Reviews*, *61*(3), 598–645.
49. Schelleis, C., Scheuring, B. M., Liebig, W. V., Hrymak, A. N., & Henning, F. (2023). Acs. *Polymers*, *15*(9), 2041.
50. Scheuring, B., Christ, N., Blarr, J., Liebig, W., Hohe, J., Montesano, J., & Weidenmann, K. A. (2024). Experimental and homogenized orientation- dependent properties of hybrid long fiber-reinforced thermoplastics. *International Journal of Mechanical Sciences*, *280*, 109470.
51. Pinter, P., Dietrich, S., Bertram, B., Kehrer, L., Elsner, P., & Weidenmann, K. (2018). Comparison and error estimation of 3d fibre orientation analysis of computed tomography image data for fibre reinforced composites. *NDT & E International*, *95*, 26–35.
52. Blarr, J., Sabiston, T., Krauß, C., Bauer, J. K., Liebig, W., Inal, K., & Weidenmann, K. A. (2023). Implementation and comparison of algebraic and machine learning based tensor interpolation methods applied to fiber orientation tensor fields obtained from CT images. *Computational Materials Science*, *228*, 112286.
53. Walpole, L. (1969). On the overall elastic moduli of composite materials. *Journal of the Mechanics and Physics of Solids*, *17*(4), 235–251.
54. Walpole, L. (1966). On bounds for the overall elastic moduli of inhomogeneous systems–I. *Journal of the Mechanics and Physics of Solids*, *14*(3), 151–162.
55. Advani, S. G., & Tucker III, C. L. (1987). The use of tensors to describe and predict fiber orientation in short fiber composites. *Journal of Rheology*, *31*(8), 751–784.
56. Böhlke, T., & Brüggemann, C. (2001). Graphical representation of the generalized Hooke's law. *Technische Mechanik*, *21*(2), 145–158.
57. Trauth, A., Kehrer, L., Pinter, P., Weidenmann, K., & Böhlke, T. (2021). On the effective elastic properties based on mean-field homogenization of sheet molding compound composites. *Composites Part C: Open Access*, *4*, 1–8.

How to cite this article: Kehrer, L., Scheuring, B., Blarr, J., & Böhlke, T. (2024). Hydrothermal behavior of pure PA 6 and homogenization of discontinuous long carbon fiber-reinforced PA 6. *Proceedings in Applied Mathematics and Mechanics*, e202400135. https://doi.org/10.1002/pamm.202400135